Direct and highly selective conversion of captured CO_2 into methane through integrated carbon capture and utilization over dual functional materials

Hongman Sun[a,b], Yu Zhang[c], Shaoliang Guan[d,e], Jun Huang[f,*]and Chunfei Wu[a,b,g,*]

[a] *School of Chemistry and Chemical Engineering, Queen's University Belfast, Belfast, BT7 1NN, UK*

[b] *School of Engineering and Computer Science, University of Hull, Hull HU6 7RX, UK*

[c] *School of Science, China University of Petroleum (East China), Qingdao, 266580, China*

[d] *Cardiff Catalysis Institute, School of Chemistry, Cardiff University, Cardiff, CF10 3AT, UK*

[e] *Harwell XPS, Research Complex at Harwell, Rutherford Appleton Laboratory, Didcot, OX11 0FA, UK*

[f] *School of Chemical and Biomolecular Engineering, the University of Sydney, Sydney, NSW 2037, Australia*

[g] *School of Energy and Environmental Engineering, Hebei University of Technology, Tianjin, 300401, China*

** Corresponding authors: E-mail: c.wu@qub.ac.uk (C. Wu); jun.huang@sydney.edu.au (J. Huang).*

ABSTRACT

Excessive atmospheric CO_2 emission is regarded as one of the main factors causing global climate change. Thus, there is an urgent need to explore the possibility of CO_2 capture and converting the captured CO_2 to fuels or value-added products. Recently, an integrated carbon capture and utilization (ICCU) process performed in a single reactor under isothermal conditions draws intensive attentions due to the reduction of energy requirement for sorbent regeneration. However, from literature, normally a low loading of sorbent in dual functional materials (DFMs) was applied resulting in a very low CO_2 capture capacity and consequent low CH_4 yield in the ICCU process. Herein, we demonstrate the intermediate-temperature DFMs using inexpensive high-capacity MgO sorbent. The synthesized DFMs are a physical mixture of sorbent and Ru/CeO_2 catalyst by the mass ratio of 2:1 allowing simultaneous regeneration of sorbent and conversion of CO_2 in a single reactor at 300 ˚C. During the 1st cycle of ICCU process, $10Ru/CeO_2$-MgO exhibits the best ICCU performance with the highest CH_4 yield of 7.07 mmol g^{-1} and CO_2 conversion of 89%. However, after 10 cycles of ICCU process, $5Ru/CeO_2$-MgO exhibits the highest CH_4 yield (3.36 mmol g^{-1}) and CO_2 conversion (79%), which are much higher than that of $2.5Ru/CeO_2$-MgO (1.14 mmol g^{-1} and 39%) and $10Ru/CeO_2$-MgO (2.31 mmol g^{-1} and 69%). It is mainly attributed to that more oxygen vacancies are remained in $5Ru/CeO_2$-MgO resulted from the metal-support interaction.

Keywords: sorbent; catalysts; CO_2 capture and conversion; the Sabatier reaction; methane

1. Introduction

The earth's surface temperature exhibited a dramatic increase and will increase continually due to the anthropogenic CO_2 emissions [1, 2]. Thus, many efforts are being made to developing new

technologies for carbon dioxide mitigation [3, 4]. Carbon capture and utilization (CCU) is a very promising strategy to reduce CO_2 emissions due to CO_2 acting as the carbon source can be used to produce value-added products [5, 6]. However, the current state-of-art of CCU has several steps including CO_2 capture, the regeneration of sorbent, and the conversion of captured CO_2. The transportation of sorbent from carbon capture reactor to sorbent regeneration reactor using temperature swing process has caused significant challenges e.g. sorbent attrition [7]. Recently, an integrated carbon capture and utilization (ICCU) process has been proposed to combine the regeneration of sorbent and catalytic conversion of the captured CO_2 in a single fixed bed reactor under isothermal conditions [8-10], which can reduce the energy required for sorbent regeneration, the infrastructure to transport and store captured CO_2.

The reverse water-gas shift (RWGS) as shown in Eq.(1) is a promising reaction for the utilization of CO_2 because carbon monoxide (CO) acts as a feedstock to produce fuels and chemicals via Fischer-Tropsch process [11, 12]. In our previous work, the ICCU process has been proven for the CO production [8]. The captured CO_2 was converted into CO in a single reactor under isothermal conditions using one-pot method synthesized DFMs, which exhibited a good stability after 20 cycles of ICCU process. In addition, dry reforming of methane or ethane has also attracted significant attentions because these two processes can convert two major greenhouse gases including CO_2 and CH_4 or C_2H_6 into a mixture of CO and H_2 (Eq. (2) or Eq. (3), respectively) [13, 14].

$$CO_2+H_2 \leftrightarrow CO+H_2O,\ \Delta H_{r,298K} = +41.2\ \text{kJ mol}^{-1} \quad (1)$$

$$CO_2+CH_4 \leftrightarrow 2CO+2H_2,\ \Delta H_{r,298K} = +247\ \text{kJ mol}^{-1} \quad (2)$$

$$2CO_2+C_2H_6 \leftrightarrow 4CO+3H_2,\ \Delta H_{r,298K} = +429\ \text{kJ mol}^{-1} \quad (3)$$

Recently, the Sabatier reaction (Eq. (4)) has attracted considerable attention due to the existence of infrastructure for CH_4 applications and environmental benefits [15, 16]. CO_2 methanation is strongly exothermic (ΔH=-164 kJ mol^{-1}) and limited by thermodynamics at high temperature. Relatively mild reaction conditions can not only maximize the reaction conversion but also largely increase the selectivity of CH_4 due to avoiding the formation of by-product such as CO [17]. Various metals (Ni, Pt, Rh, and Ru) and supports (CeO_2, TiO_2, Al_2O_3, SiO_2, and ZrO_2) have been extensively investigated for CO_2 methanation [18]. At a low operating temperature, it is found that Ru is highly active and selective to methane, especially when it is supported on reducible supports (CeO_2, TiO_2, ZrO_2) [19, 20]. Duyar et al. successfully captured CO_2 from flue gas and converted the captured CO_2 to natural gas at 320 ˚C sequentially in the same reactor by DFMs, which consist of nano-dispersed CaO and Ru acting as sorbent and methanation catalyst, respectively [5]. Bermejo-López et al. investigated the utilization of Na_2CO_3 as the sorbent to convert the captured CO_2 to

CH_4 and proposed a mechanism of CO_2 capture and hydrogenation process [21]. However, a low loading of sorbent in this integrated process resulted in a very low CO_2 uptake and consequent low CH_4 production. In addition, the desired temperature of Ru in Sabatier reaction is around 300 ˚C, which is much lower than the temperature of carbon capture using CaO-based materials (normally 600 ˚C and 900 ˚C for carbonation and regeneration, respectively) [22]. Therefore, the consistency of carbon capture temperature using the sorbent and conversion temperature using catalytic sites is very important for the synthesis of DFMs. Further increasing the loading of sorbent is also crucial important.

$$CO_2+4H_2 \leftrightarrow CH_4+2H_2O,\ \Delta H_{r,298K}= -164\ kJ\ mol^{-1} \quad (4)$$

Magnesium oxide (MgO) appear to be particularly advantageous in ICCU process because the temperature for carbon capture is around 300 ˚C, which is also a desirable temperature for CO_2 methanation using Ru-based catalysts [23]. However, pure MgO exhibits a moderate CO_2 capture capacity, which is normally lower than 1 mmol g^{-1} and poor thermal stability during the cyclic performance of sorbent [24]. Recently, incorporating alkali metal nitrates into MgO molten state received intensive attention to improve CO_2 capture capacity [24, 25]. This is attributed to the introduction of molten nitrates into MgO sorbent can prevent the generation of rigid CO_2-impermeable product layer of unidentate carbonates on the surface of MgO and then promote the formation of carbonate ions (CO_3^{2-}) in the molten salts [24]. Therefore, we synthesised an inexpensive high-capacity MgO sorbent modified by the alkali metal nitrates.

Here, we develop Ru/CeO_2-MgO as DFMs, which is a physical mixture of an inexpensive high-capacity MgO sorbent and a Ru/CeO_2 catalyst with the mass ratio of 2:1. CeO_2 nanorods are used as Ru support as the reaction rate can be dramatically improved by the oxygen vacancies on the surface of CeO_2 through absorbing and activating the carbon-oxygen bond [20]. The schematic diagram of the proposed ICCU process using the synthesized Ru/CeO_2-MgO DFMs is displayed in Fig. 1. This ICCU process has two steps. The first step is CO_2 capture from flue gas using high-capacity MgO sorbent. The second step is converting the captured CO_2 into CH_4 using Ru/CeO_2 catalysts in a single reactor at the same temperature via Eq. (5) after switching the feed gas to renewable H_2.

$$MgCO_3+4H_2 \leftrightarrow MgO+CH_4+2H_2O,\ \Delta H_{r,298K}= -67\ kJ\ mol^{-1} \quad (5)$$

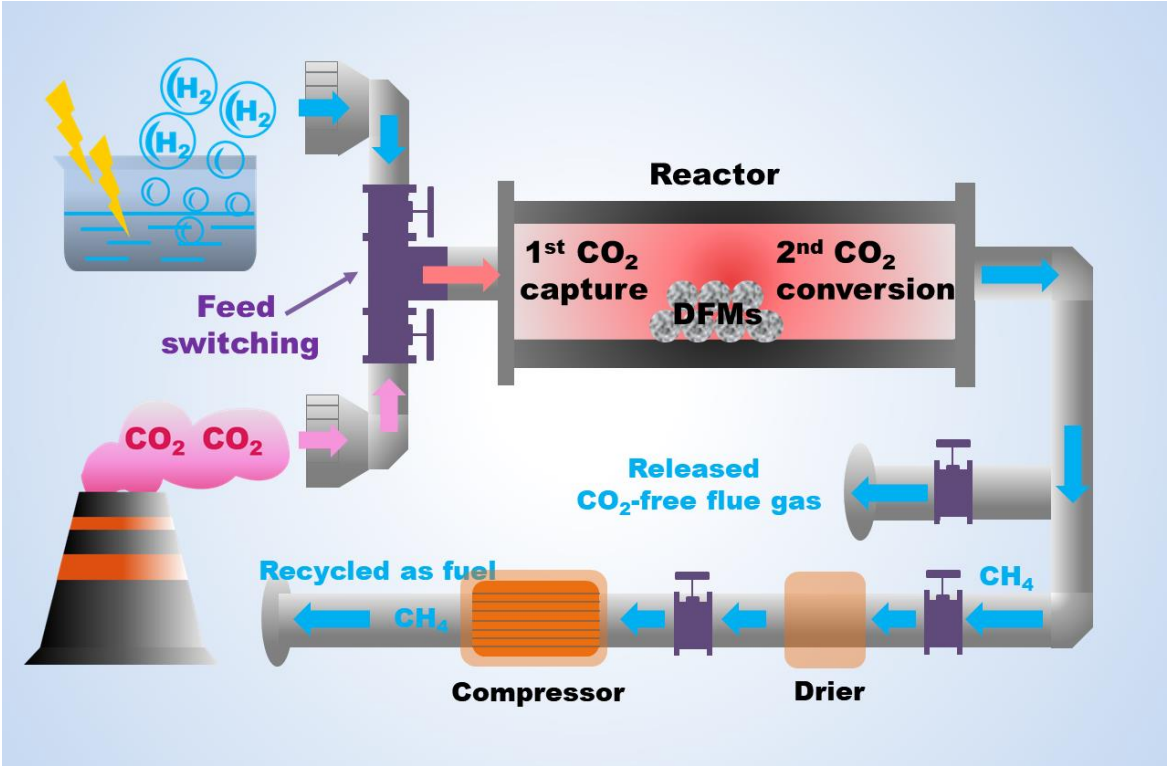

Fig. 1. Schematic diagram of ICCU process directly converting the captured CO_2 into methane over DFMs.

2. Experimental section

2.1. Preparation of Catalyst

A hydrothermal process as previously reported was used to synthesize CeO_2 nanorods [26]. Typically, 1.730 g of $Ce(NO_3)_3 \cdot 6H_2O$ and 28.0 g of NaOH were dissolved in 10 mL and 70 mL of deionized water, respectively. These two solutions were mixed in a plastic beaker and stirred for 30 min to form light purple slurry. After that, the mixture was transferred into a stainless-steel autoclave (100 mL) and put into the oven at 120 ˚C for 24 h. After cooling down to the room temperature, the white precipitates were filtered using vacuum pump and washed until the pH reached 7 with deionized water and ethanol. The obtained yellow powder was dried at 80 ˚C overnight and calcined at 600 ˚C for 5 h.

Ru/CeO_2 catalyst was prepared by a wet impregnation method using the synthesized CeO_2 nanorods as the support. Typically, 0.5 g CeO_2 nanorods were added into 20 mL solution with predetermined amount of $RuCl_3$, corresponding to 2.5wt%, 5wt% and 10wt% of Ru. The black slurry was stirred for 24 h at room temperature and then evaporated water at 80 ˚C. After that, the obtained black powder were dried at 100 ˚C overnight, calcined at 300 ˚C for 2 h and reduced at 300 ˚C for 2 h in 5% H_2/N_2 with a flow rate of 50 mL min^{-1}. The synthesized catalysts are donated as $2.5Ru/CeO_2$, $5Ru/CeO_2$ and $10Ru/CeO_2$.

2.2. Preparation of DFMs

High-capacity MgO sorbent was prepared as reported by Harada et al. [24]. Typically, 9.713 g of $4MgCO_3 \cdot Mg(OH)_2 \cdot 5H_2O$ and 0.207 g of $LiNO_3$, 0.153 g of $NaNO_3$, and 0.526 g of KNO_3 were added in 40 mL of deionized water at room temperature and stirred for 60 min. The obtained white slurry was dried at 120 ˚C overnight and then calcined at 450 ˚C for 4 h.

The fabrication of DFMs was performed by physically mixing high-capacity MgO sorbent and reduced Ru/CeO_2 catalysts by the mass ratio of 2:1.

2.3. Material characterization

The loading of Ru on CeO_2 nanorods was determined by inductively coupled plasma-optical emission spectroscopy (ICP-OES, 5300DV). Nitric acid was utilized to dissolve the catalysts. Firstly, the samples which are dissolved into the nitric acid are heated in the microwave to 180 ˚C and held for 10 min. After that, it was cool down to room temperature. Powder X-ray diffraction (XRD) patterns ranging from 10 to 80˚ were collected by a PANalytical empyrean series 2 diffractometer with Cu Ka X-ray source. Scherrer's equation was utilized to calculate the average crystallite size of CeO_2 nanorods based on the diffraction peaks at 28.5˚. BET surface area was measured by ASAP 3000 analyser at 77 K. The Brunauer-Emmett-Teller (BET) surface area was calculated by the adsorption branch data when the relative pressure (P/P_0) ranges from 0.06 to 0.2. Scanning electron microscopy (SEM) images coupled with an energy dispersive X-ray spectrometer (EDX) were measured by Stereoscan 360. Transmission electron microscopy (TEM, JEOL 2010) and high-resolution TEM (HRTEM, FEI talos F200) are utilized to observe the detailed structure of DFMs. The samples which are dispersed in acetone uniformly were dropped on Cu grids coated with carbon and dried for TEM characterization. Valence states on the surface of Ru/CeO_2 catalysts and spent DFMs were acquired by X-ray photoelectronic spectrometer (XPS, Escalab 250Xi) using Mg Kα radiation. The binding energies were calibrated by the C1s peak centred at 284.8 eV of adventitious carbon. CO_2 temperature-programmed desorption (CO_2-TPD), H_2 temperature-programmed reduction (H_2-TPR) and CO chemisorption of Ru/CeO_2 catalysts were characterized by the Micromeritics Autochem II 2920 analyser. The catalyst around 100 mg was placed in a U-shape tube and pre-treated at 100 ˚C in the inert gas to remove absorbed gases and moisture. For CO_2-TPD, CO_2 adsorption was conducted in 10% CO_2/He. CO_2 desorption was conducted with the temperature increasing from 50 ˚C to 800 ˚C. For H_2-TPR, after the temperature of U-shape tube decreased to 50 ˚C, the catalyst was reduced with the temperature ranging from 50 ˚C to 800 ˚C at a heating rate of 10 ˚C min^{-1} in 5% H_2/N_2 (30 mL min^{-1}). For CO chemisorption, firstly, the catalyst was reduced in 10% H_2/Ar at 300 ˚C for 2 h and then the U-shape tube was purged by pure He at 350 ˚C for 30 min. After cooling down to 50 ˚C, the chemisorption was performed in 10% CO/He.

The Raman spectra were collected using 532 nm as the excitation wavelength and 1 cm^{-1} as the resolution.

2.4. Integrated CO_2 capture and utilization

A fixed-bed reactor coupled with an online gas analyser purchased from ETG Risorse & Tecnologia as shown in Fig. S1 (Supporting Information, SI) was utilized for the evaluation of ICCU performance of synthesized DFMs. The length and inner diameter of stainless steel tube in this fixed bed reactor is 50 cm and 0.635 cm, respectively. Typically, 450 mg of powdered DFMs was placed in the middle of the reactor and two ends were fixed by quartz wool. The carbonation reaction (carbon capture stage) was performed in 65% CO_2/N_2 (50 mL min^{-1}) at 300 ˚C for 60 min. Then, the reactor was purged by pure N_2 for 5 min. The second stage is converting the captured CO_2 into CH_4 at the same temperature after switching the feed gas to renewable H_2 (5% H_2/N_2) with a flow rate of 50 mL min^{-1}. In total, 10 cycles of ICCU process were conducted as the description. The calculation of carbon balance and CO_2 conversion are shown in supporting information.

The mechanism study of ICCU process was investigated by in-situ DRIFTS (Spectro-meter: JASCO-4600, DRIFTS cell: Bruker). The first step is carbon capture from 65% CO_2/N_2 at 300 ˚C for 60 min. Then, the DRIFTS cell was purged by pure N_2 for 5 min. The conversion of captured CO_2 into CH_4 at the same temperature was conducted after switching the feed gas to 5% H_2/N_2 (50 mL min^{-1}). The spectra ranging from 4000 to 400 cm^{-1} were collected with a resolution of 4 cm^{-1}.

3. Results and discussions

3.1. Characterization of fresh catalysts

The elemental analysis of pristine CeO_2 and reduced Ru/CeO_2 catalysts is studied by ICP-OES. The obtained results are summarised in Table 1. It is found that there are no Ru species in pristine CeO_2, which is consistent with the predetermined metal contents. After impregnating Ru on CeO_2 nanorods, the percentage of Ru element is calculated as 3.52%, 6.60% and 12.75%, respectively, which are used to investigate the influence of Ru loadings in the ICCU process.

Table 1 Elemental analysis and average crystallite size of reduced catalysts.

Samples	Ru element percentage[a] (%)	CeO_2[b] (nm)	S_{BET}[c] (m^2 g^{-1})	Ru dispersion[d] (%)
CeO_2	0	15.6	42	/
2.5Ru/CeO_2	3.52	18.3	42	61.28
5Ru/CeO_2	6.60	16.9	40	23.69
10Ru/CeO_2	12.75	16.8	27	5.29

[a] Element percentage calculated from ICP results.

[b] Average crystallite size obtained from Scherrer's equation.

[c] BET surface area.

[d] Ru dispersion obtained from CO chemisorption.

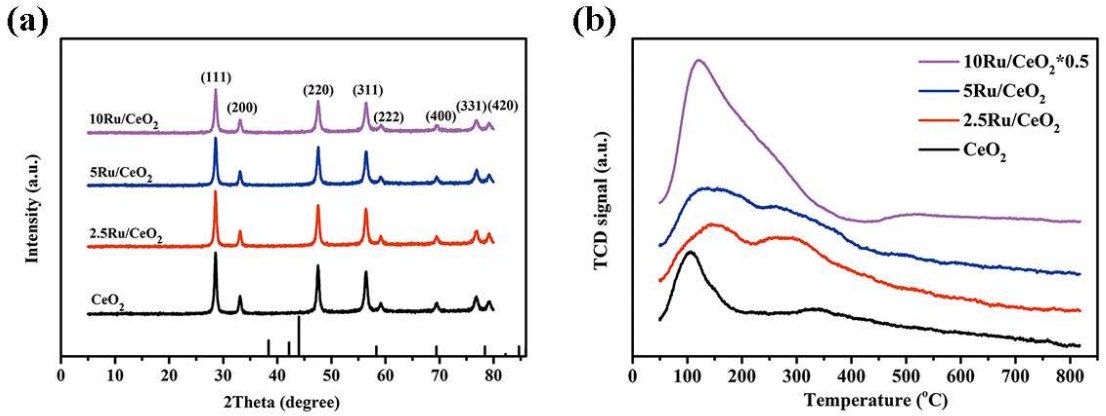

Fig. 2. XRD patterns (a) and CO_2-TPD profiles (b) of CeO_2 nanorods and Ru/CeO_2 catalysts.

The X-ray diffractogram of reduced pristine CeO_2 nanorods and Ru/CeO_2 catalysts with different Ru loadings, as well as the reference peak positions of hcp-structured Ru (JCPDS 6-0663) is presented in Fig. 2. The peaks centred at 28.5˚, 33.2˚, 47.6˚, 56.5˚, 59.2˚, 69.4˚, 76.7˚ and 79.1˚ are assigned to the lattice plane of (111), (200), (220), (311), (222), (400), (331) and (420), respectively in the cubic structure of CeO_2 (JCPDS 34-0394) [19]. The average CeO_2 crystallite size is calculated as 15.6, 18.3, 16.9, 16.8 nm for CeO_2, 2.5Ru/CeO_2, 5Ru/CeO_2 and 10Ru/CeO_2, respectively, using Scherrer's equation. However, no distinct diffraction peaks belonging to Ru or RuO_2 species can be detected in the reduced and non-reduced Ru/CeO_2 catalysts, respectively in Fig. 2 and Fig. S2. This indicates that the Ru active sites are well dispersed on CeO_2 nanorods or partly incorporated into the lattices of CeO_2 nanorods [27].

CO_2-TPD profiles of pristine CeO_2 and Ru/CeO_2 catalysts are displayed in Fig. 2b. Two CO_2 desorption peaks centred at 106 ˚C and 324 ˚C are attributed to the weak and strong CO_2 chemisorption, respectively indicating the basic property of CeO_2 nanorod as reported in the previous study [28]. With the increase of Ru loading, the intensity of CO_2 desorption peaks is increased, which implies the Ru species can enhance the basic sites and resulting a better CO_2 adsorption ability.

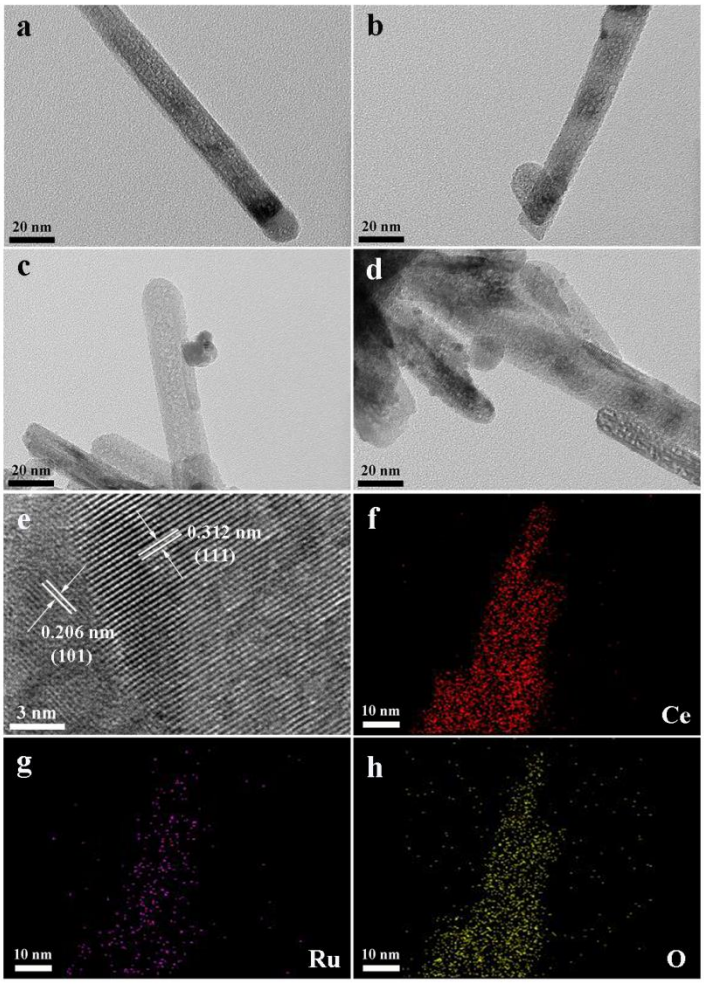

Fig. 3. TEM images of reduced catalysts CeO_2 (a), 2.5Ru/CeO_2 (b), 5Ru/CeO_2 (c) and 10Ru/CeO_2 (d). HRTEM (e) and element mapping (f-h) of reduced 5Ru/CeO_2.

SEM images of the synthesized Ru/CeO_2 catalysts and corresponding element mapping of 5Ru/CeO_2 are shown in Fig. S3. It is found that the Ru/CeO_2 catalysts can inherit the original morphology of CeO_2 after introducing Ru active sites. The detailed morphologies and active components of CeO_2 support and Ru/CeO_2 are determined by TEM and HRTEM, as well as element mapping analysis as displayed in Fig. 3. The width and length of the well-crystallized CeO_2 nanorods prepared by the hydrothermal method is ranging from 10 to 20 nm and 100 to 200 nm, respectively, as shown in Fig. 3a. The EDX spectrum as shown in Fig. S4 proves the successful introduction of Ru species on CeO_2 support. As for the reduced 5Ru/CeO_2, the interplanar spacing of 0.206 nm and 0.312 nm represent lattice plane (101) of Ru and (111) of CeO_2, respectively [29]. The element mappings of 5Ru/CeO_2 as shown in Fig. 3f-h and Fig. S3e-f demonstrate the uniform distribution of Ce, Ru and O elements, which is important to prevent the aggregation of Ru species. In addition, with the further increase of Ru loadings, the length of CeO_2 nanorods and the surface

area are decreased as shown in Fig. 3c, d and Table 1. In addition, 2.5Ru/CeO_2 exhibits a much higher Ru dispersion (61.28%) than that of 5Ru/CeO_2 and 10Ru/CeO_2 from the CO chemisorption results in Table 1.

3.2. Oxygen vacancies of fresh catalysts

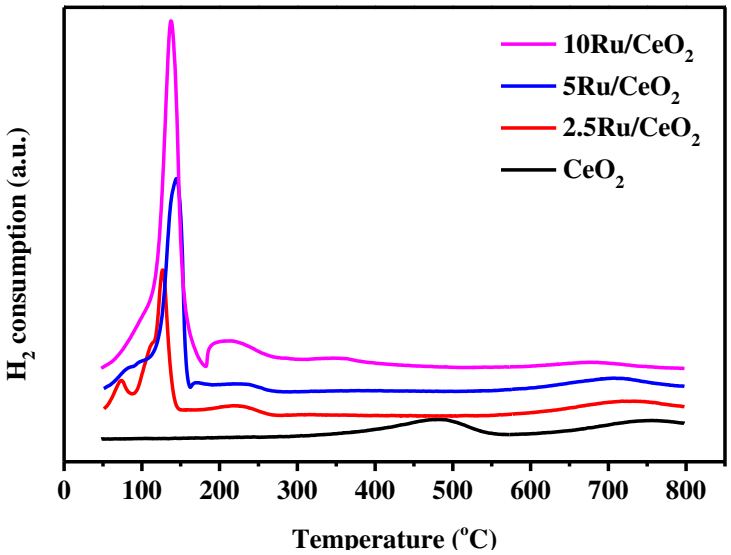

Fig. 4. H_2-TPR profiles of CeO_2, 2.5Ru/CeO_2, 5Ru/CeO_2 and 10Ru/CeO_2.

The close relationship between metal-support interaction and oxygen vacancies has received intensive attention due to the promotion for the catalytic reaction [30]. Therefore, a further insight of the mentioned relationship was studied using TPR, Raman and XPS. The reducibility of CeO_2 support and Ru/CeO_2 catalysts is studied by H_2-TPR in Fig. 4. In the reduction process of CeO_2 support, the temperature below 500 ˚C and higher than 700 ˚C is normally attributed to the reduction of surface CeO_2 and bulk CeO_2, respectively [27]. For the Ru/CeO_2 catalyst, there is a shoulder peak lower than 100 ˚C due to the oxygen adsorption [26]. Two other peaks centred at 120-160 ˚C (peak I) and 200-260 ˚C (peak II) are observed, which are attributed to the interaction between RuO_x species and CeO_2 supports [27]. The temperature of peak I is gradually decreased from 138 ˚C in 10Ru/CeO_2 to 128 ˚C in 2.5Ru/CeO_2, which is attributed to the reducibility was improved [31]. Compared to pristine CeO_2, ceria support in Ru/CeO_2 catalyst exhibits a lower reduction temperature, indicating that the introduction of Ru species promote the reduction of ceria. In addition, a quantitative H_2 consumption for RuO_2 reduction as shown in Table 2 greatly exceeds the stoichiometric H_2 consumption for the complete reduction of RuO_2 (15.0 mmol/g RuO_2). This phenomenon indicates that a large amount of H_2 is used to remove the surface oxygen of ceria and sequentially generate the oxygen vacancies [32].

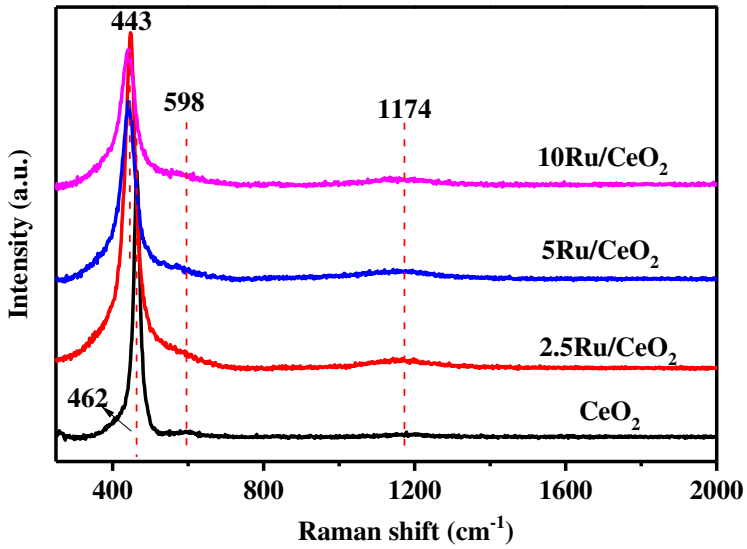

Fig. 5. Visible Raman spectra of CeO_2, 2.5Ru/CeO_2, 5Ru/CeO_2 and 10Ru/CeO_2.

Except for the metal active sites, the oxygen vacancies in the Ru/CeO_2 catalysts may serve as an important cooperative site for CO_2 conversion. Raman spectra are employed to investigate the concentration and formation of oxygen vacancies as shown in Fig. 5. The sharp peak at 462 cm^{-1} indicates the presence of vibration mode of octahedral local symmetry around CeO_2 lattice (F_{2g}). Another peak at 598 cm^{-1} is assigned to the defect-induced (D) mode in CeO_2 phase. After the introduction of Ru active species, those Raman peaks remained. However, compared to the pristine ceria, the peak corresponding to F_{2g} exhibited a red shift, which is attributed to the presence of oxygen vacancies derived from the introduction Ru into CeO_2 nanorods [33]. In addition, another weak peak centred at 1174 cm^{-1} is attributed to the second-order longitudinal modes of CeO_2 [34]. The intensity ratio of I_D/I_{F2g} is defined as the concentration of oxygen vacancies in CeO_2, which increases in the order of CeO_2 (0.018) < 2.5Ru/CeO_2 (0.047) < 5Ru/CeO_2 (0.051) < 10Ru/CeO_2 (0.072) as shown in Table 2. Importantly, the I_D/I_{F2g} ratio increases significantly due to the addition of Ru on the CeO_2 nanorod support, which indicates the crucial role of the H_2 reduction in the formation of oxygen vacancies.

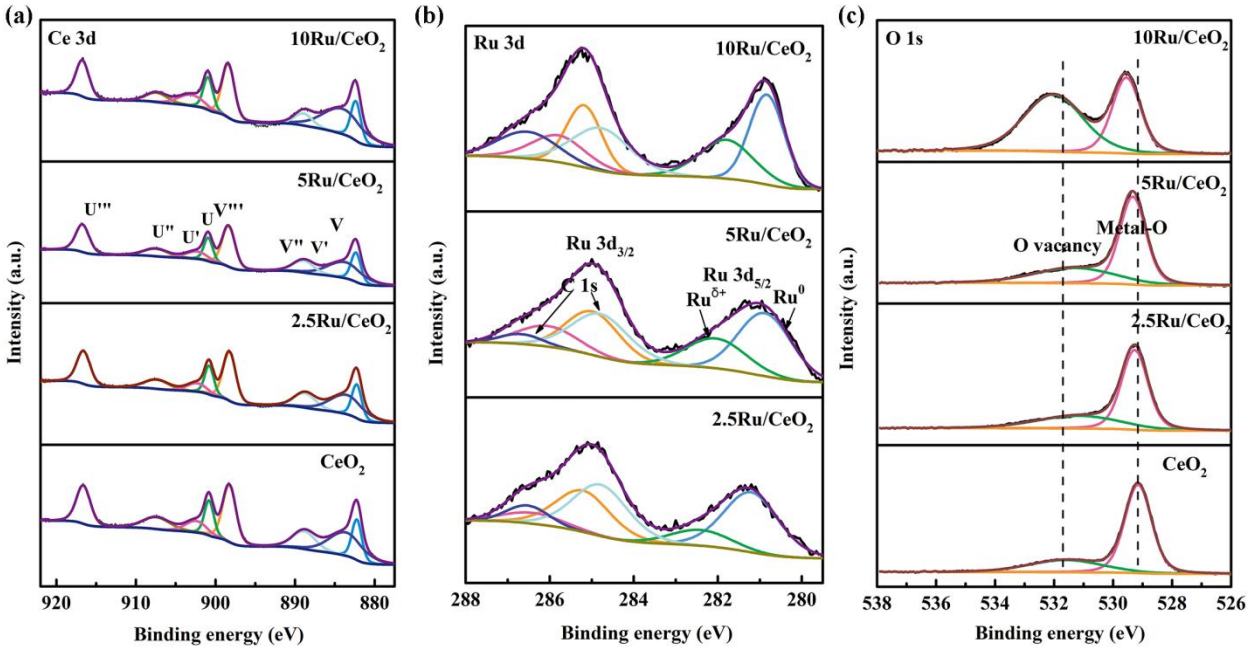

Fig. 6. XPS spectra and peak fitting curves Ce 3d (a), Ru 3d (b) and O 1s (c) of reduced catalysts.

Table 2 TPR, Raman and XPS data of the reduced CeO_2 and Ru/CeO_2.

Sample	H_2 consumption[a]	Raman	Ru 3d	Ce 3d	O 1s
	(mmol/g RuO_2)	I_D/I_{F2g}	$Ru^{\delta+}/(Ru^{\delta+}+Ru^0)$	Ce^{3+}/Ce^{4+}	O_V/O_L
CeO_2	/	0.018	/	0.37	0.38
2.5Ru/CeO_2	25.6	0.047	0.22	0.37	0.51
5Ru/CeO_2	20.9	0.051	0.35	0.39	0.53
10Ru/CeO_2	20.4	0.072	0.41	0.56	1.56

[a] H_2 consumption calculated by H_2-TPR

XPS spectra for the pristine CeO_2 and Ru/CeO_2 catalysts are conducted for the study of valence states and chemical composition and the results are displayed in Fig. 6. Eight main binding energy peaks can be observed in Fig. 6a. The six peaks centred at 916.3, 907.4, 900.6, 898.0, 888.9 and 881.8 eV are assigned to Ce^{4+}, and the two peaks centred at 902.4 and 883.6 eV are ascribed to Ce^{3+} [35]. The ratios of Ce^{3+} to Ce^{4+} are increased with the increase of Ru loadings as shown in Table 2 indicating that more oxygen vacancies are generated on the surface of CeO_2 nanorods.

The peaks of Ru 3d are deconvoluted to analyse the Ru species in different oxidation states, which are mainly composed of Ru^0 and $Ru^{\delta+}$ from Ru nanoparticles and the interface between Ru and CeO_2, respectively [27]. The existence of $Ru^{\delta+}$ species is caused by the metal-support interaction with the electrons transferring from Ru to CeO_2 support as shown in Eq. (6), which could result in a better catalytic performance. The percentage of $Ru^{\delta+}$ is increased from 22% in 2.5Ru/CeO_2 to 41%

in 10Ru/CeO_2 implying that the catalytic activity would be enhanced with the increase of Ru loading.

$Ru^0+{}^{\delta}Ce^{4+} \rightarrow Ru^{\delta+}+{}^{\delta}Ce^{3+}$ (6)

The presence of oxygen vacancies in the synthesized catalysts is further proved by O 1s spectra as shown in Fig. 6c. The peak at ~529.1 and ~531.8 eV is assigned to the lattice oxygen (O_L) and oxygen deficient regions (O_V), respectively. As shown in Table 2, with the increase of Ru loading, O_V/O_L exhibits an obvious increase which confirms the more oxygen vacancies are generated in a higher Ru loading catalyst [36, 37]. It agrees with the enhancement of Ce^{3+} and $Ru^{\delta+}$ peaks.

3.3. Integrated CO_2 capture and utilization performance

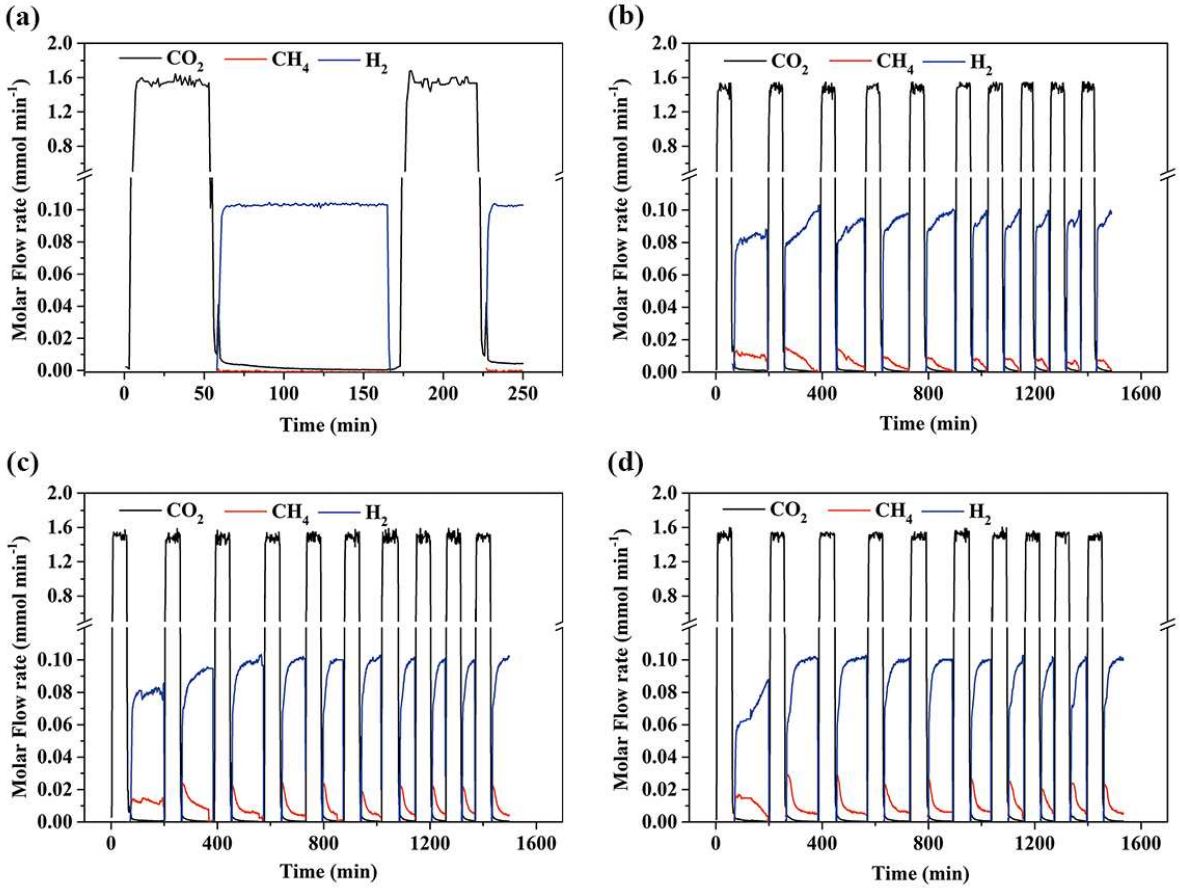

Fig. 7. ICCU performance of CeO_2-MgO (a); 2.5Ru/CeO_2-MgO (b); 5Ru/CeO_2-MgO (c) and 10Ru/CeO_2-MgO (d).

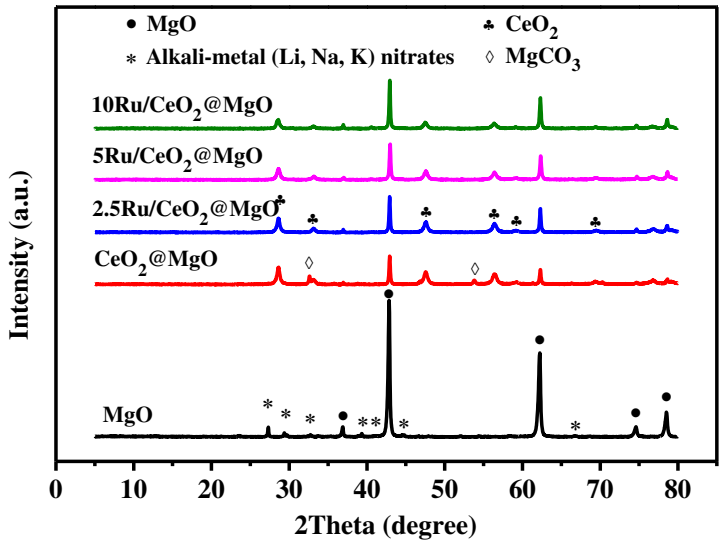

Fig. 8. XRD patterns of MgO and spent DFMs (CeO_2-MgO is after 2 ICCU cycles and others are after 10 ICCU cycles).

The ICCU performance of various DFMs is displayed in Fig. 7 and Table S1-3. As a comparison, CeO_2-MgO demonstrates a low activity of CO_2 hydrogenation and almost no CH_4 can be observed in the second step (switching feed gas to 5% H_2/N_2) in Fig. 7a due to the absence of Ru active sites. The captured CO_2 is considered in the form of $MgCO_3$, which is further confirmed by the $MgCO_3$ diffraction peaks centred at 32.6˚ and 53.9˚ in XRD results of the spent CeO_2-MgO sample as shown in Fig. 8. After introducing Ru species on CeO_2 nanorods, CH_4 can be clearly detected after switching to 5% H_2/N_2 in the ICCU process, and only a small amount of CO_2 and almost no CO can be observed for all the DFMs during the methanation process as shown in Fig. 7b-d. It is indicated that the captured CO_2 has been mostly utilised and converted into CH_4 when the feed gas was switched from CO_2 to 5% H_2/N_2. This is consistent with the superior methanation activity of Ru [38].

Table 3 ICCU performance of DFMs.

Samples	1st cycle			10th cycle	
	CH_4 yield[a] (mmol g^{-1})	CO_2 conversion[b] (%)	TOF[c] (h^{-1})	CH_4 yield (mmol g^{-1})	CO_2 conversion (%)
2.5Ru/CeO_2-MgO	5.73	60	113.4	1.13	39
5Ru/CeO_2-MgO	6.60	74	361.6	3.36	79
10Ru/CeO_2-MgO	7.07	89	1511.8	2.31	69

[a] calculated by per gram of sorbents

[b] CO_2 conversion= CH_4 yield/CO_2 capture capacity

[c] TOF= Number of moles of reactant consumed/ (number of active centres*reaction time)

Regarding CO_2 utilisation, the CH_4 yield, CO_2 conversion as well as TOF derived from different DFMs are summarized in Table 3. As for the 1st cycle of ICCU process, 2.5Ru/CeO_2-MgO exhibits a relatively low CH_4 yield (5.73 mmol g^{-1}) and CO_2 conversion (60%) due to the limited Ru active sites. The TOF is determined as low as 113.4 h^{-1}. With the increase of Ru loadings, the CH_4 yield and CO_2 conversion are increased to 6.60 mmol g^{-1} and 74% for 5Ru/CeO_2-MgO and further increased to 7.07 mmol g^{-1} and 89% for 10Ru/CeO_2-MgO. In addition, TOF displayed a dramatic increase after introducing Ru species and reached 1511.8 h^{-1} for 10Ru/CeO_2-MgO, which is attributed to more oxygen vacancies are generated in the sample with a higher Ru loading as proved by XPS results in Table 2.

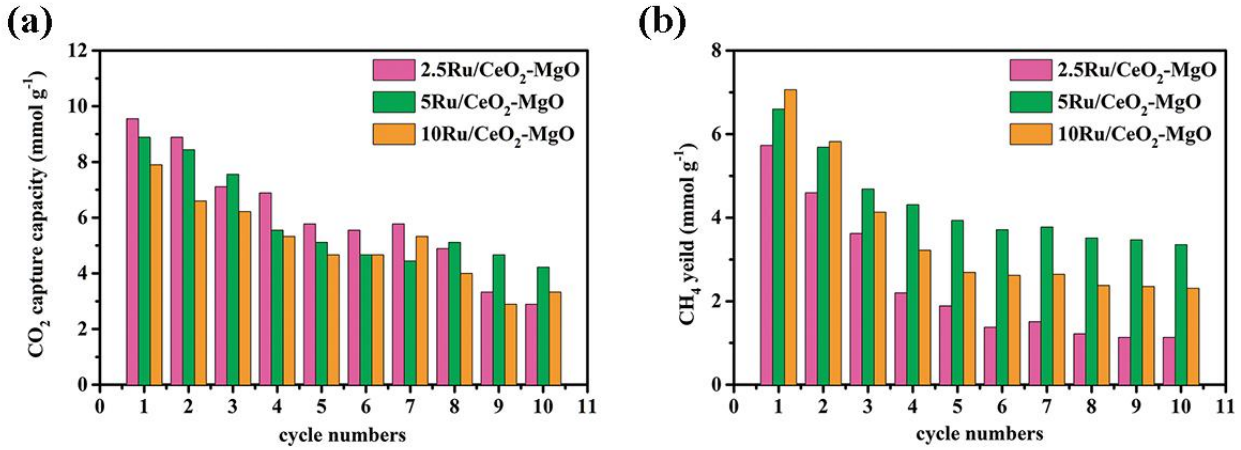

Fig. 9. Ten cycles of ICCU process of DFMs: CO_2 capture capacity (a) and CH_4 yield (b).

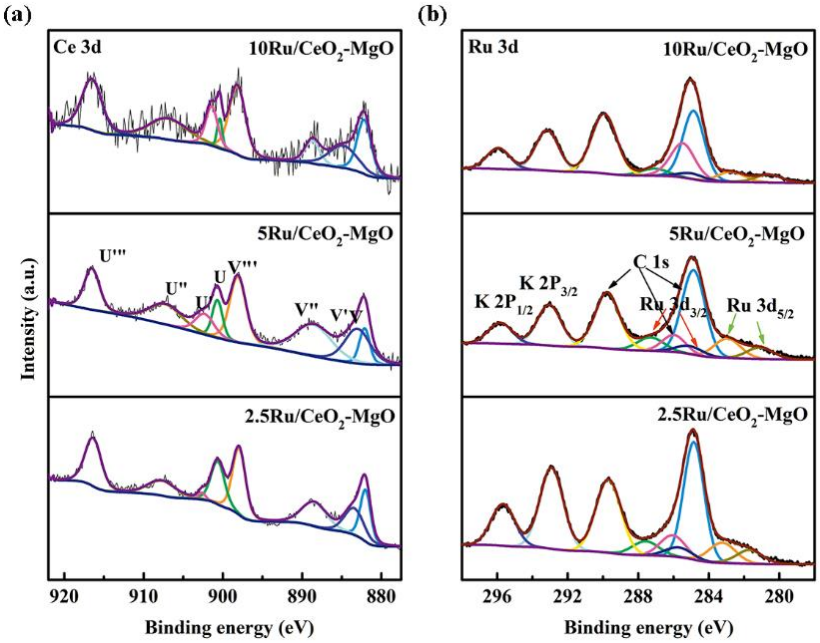

Fig. 10. XPS spectra and peak fitting curves: Ce 3d (a) and Ru 3d (b) of spent DFMs after 10 cycles of ICCU process.

The stability of synthesized DFMs are evaluated by 10 cycles of ICCU process and the results of CO_2 capture capacity and CH_4 yield are presented in Fig. 9. After 10 cycles of ICCU process, all these DFMs exhibit a decrease of CH_4 yield and CO_2 conversion as shown in Table 3 due to the sintering of MgO sorbent. This is further demonstrated in Fig. S5. The CH_4 yield obtained from 2.5Ru/CeO_2-MgO drops from 5.73 mmol g^{-1} to 1.13 mmol g^{-1} after 10 cycles of ICCU as shown in Fig. 9b. Even though 10Ru/CeO_2-MgO exhibits the best performance in the 1st cycle of ICCU process due to more oxygen vacancies, CO_2 capture capacity and CH_4 yield exhibits a dramatic decrease after 10 cycles of ICCU process from 7.90 mmol g^{-1} and 7.07 mmol g^{-1} to 3.33 mmol g^{-1} and 2.31 mmol g^{-1}, respectively. In addition, the CO_2 conversion and carbon balance also decreased from 89% and 99% to 69 and 87%, respectively as shown in Table S3. Compared to 2.5Ru/CeO_2-MgO and 10Ru/CeO_2-MgO, 5Ru/CeO_2-MgO demonstrates a better stability. After 10 cycles of ICCU process, 5Ru/CeO_2-MgO exhibits the highest CH_4 yield (3.36 mmol g^{-1}) and CO_2 conversion (79%), which is more than 8 times than the performance of ICCU process reported by Bermejo-López et al. using Ru15%CaO/Al_2O_3 and Ru10%Na_2CO_3/Al_2O_3 as the DFMs [21]. The detailed comparison of ICCU process proposed in this work and reported in other literatures are summarised in Table S4. In addition, the carbon balance and CO_2 conversion reaches up to 91% and 79%, respectively, which are much better than the performance reported by Sakpal et al. (CO_2 conversion is 75%) and Dreyer et al. (CO_2 conversion and CH_4 selectivity are 55% and 98%, respectively) [19, 39] as shown in Table S5. XPS spectra are employed to the analysis of chemical states of used DFMs after 10 cycles of ICCU process as displayed in Fig. 10 and Table S6. Compared to 2.5Ru/CeO_2-MgO and 10Ru/CeO_2-MgO, spent 5Ru/CeO_2-MgO exhibits the highest ratio of Ce^{3+} to Ce^{4+} and the highest $Ru^{\delta+}$ percentage (63%) indicating more surface oxygen vacancies are generated after 10 cycles of ICCU process and resulting in a highest CH_4 yield and CO_2 conversion. This is also confirmed by the Raman spectra of DFMs after 10 cycles as shown in Fig. 11. The intensity ratio (I_D/I_{F2g} in Table S6) of spent 5Ru/CeO_2-MgO is much higher than that of spent 2.5Ru/CeO_2-MgO and 10Ru/CeO_2-MgO further indicating the existence of more oxygen vacancies.

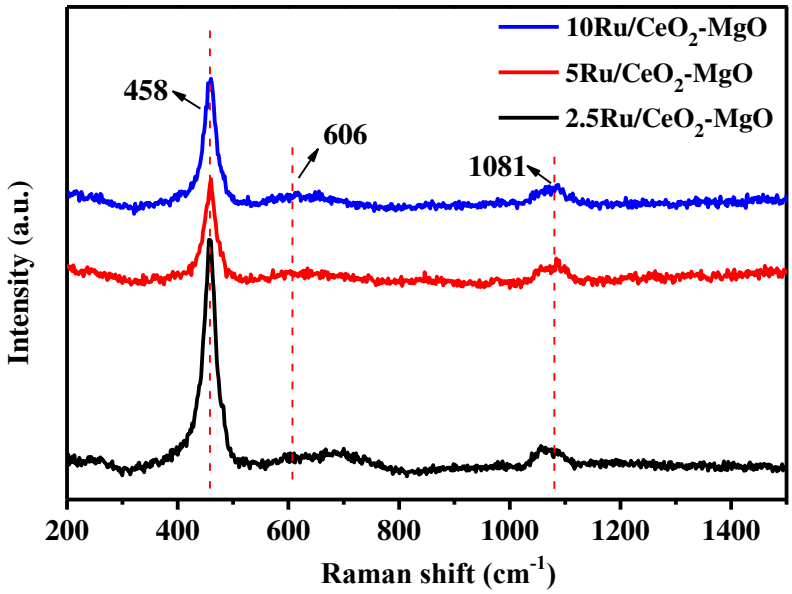

Fig. 11. Visible Raman spectra of DMFs after 10 cycles of ICCU process.

It is well accepted that the catalytic activity can be enhanced by the interaction between reducible supports and oxygen vacancies, which promote CO_2 activation and be restored through the reduction of the oxide surface [40]. The in-situ DRIFTS were further conducted for the mechanism study of ICCU process under the co-existence of Ru active sites and oxygen vacancies. As shown in Fig. 12, 1350 cm^{-1} and 1550 cm^{-1} are considered as the characteristic peaks of ν(O-C-O) in the formate species and $\nu_{as}(COO^-)$ in the carbonate species, respectively [41]. Compared to the carbon capture stage, the spectra of CeO_2-MgO after switching to H_2 for conversion remained unchanged in Fig. 12a, while the peak of 5Ru/CeO_2-MgO at 1350 cm^{-1} disappears gradually. This indicates that the formed formate species in CO_2 capture stage are consumed in the conversion reaction. Thus, formate is proposed to be the main reaction intermediate in this ICCU using the synthesized DFMs. This proposal can also be confirmed by the existence of peaks at 2032 cm^{-1} in 5Ru/CeO_2-MgO, which are attributed to the linearly adsorbed CO over the low-coordinated Ru sites [33].

The reaction mechanism for the conversion of captured CO_2 via formate route over the Ru/CeO_2 catalyst is proposed in Fig. 13. Two key steps are involved. 1) CO_2 species are activated by an oxygen vacancy and the CeO_2 nanorod is oxidised, meanwhile the Ru active site is chemisorbed with H species. The first step results in the formation of bidentate formate, which will decompose into metal carbonyl and terminal hydroxyl groups. 2) The Ru carbonyls are activated by chemically adsorbed H atoms, and finally converted to CH_4 molecules, which is a rate determining step [42]. The formed hydroxyl groups on the oxygen vacancies react with hydrogen resulting in the

formation of H_2O, which is the reduction of CeO_2 support. Therefore, the DFMs with more oxygen vacancies coupled with a good Ru dispersion exhibit a better ICCU performance.

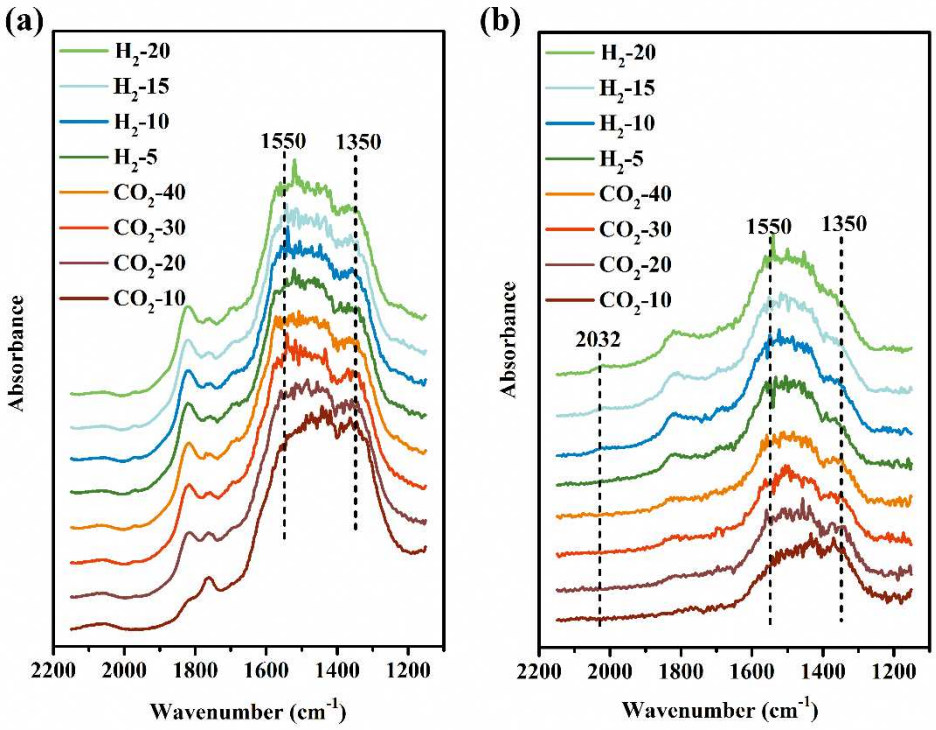

Fig. 12. In-situ DRIFTS spectra during the ICCU process over CeO_2-MgO (a) and 5Ru/CeO_2-MgO (b).

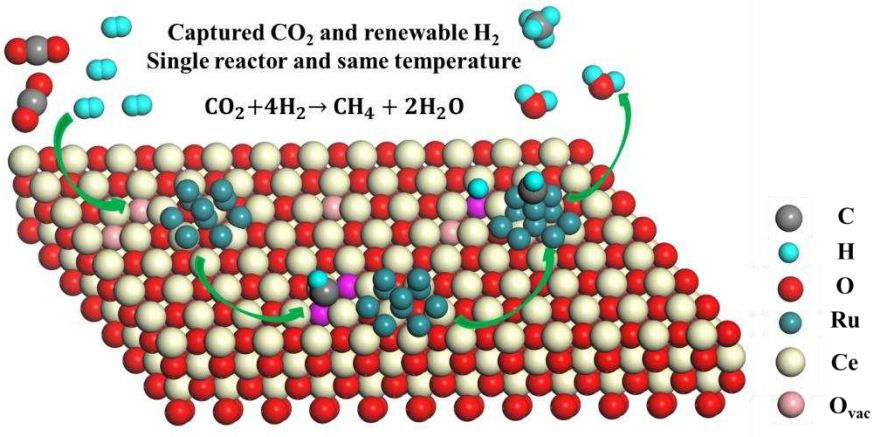

Fig. 13. Schematic illustration for the conversion of captured CO_2 via formate route over the Ru/CeO_2 catalyst.

The SEM images of spent DFMs (except for CeO_2-MgO is after 2 cycles, all other DFMs are after 10 cycles of ICCU process) and the corresponding TEM images of spent 5Ru/CeO_2-MgO have been displayed in Fig. 14. It should be noted that the rod-like material in Fig. 14a is the quartz wool used

during the ICCU process. Nanorods can be observed on the surface of spent CeO_2-MgO, indicating that CeO_2-MgO can inherit its original morphology. Compared to the bulk structure of spent 2.5Ru/CeO_2-MgO and 10Ru/CeO_2-MgO, the spent 5Ru/CeO_2-MgO catalyst after 10 cycles of ICCU process exhibits a loose structure in Fig. 14c indicating the sintering resistance, which is also confirmed by the uniform mixture of MgO sorbent and CeO_2 nanorods as shown in Fig. 14e and f (TEM images) [43]. Therefore, compared to both the traditional CO_2 methanation and ICCU process reported in the previous literatures, the ICCU process using MgO and Ru as the sorbent and active site, respectively demonstrates a high CO_2 conversion and CH_4 selectivity coupled with a good stability.

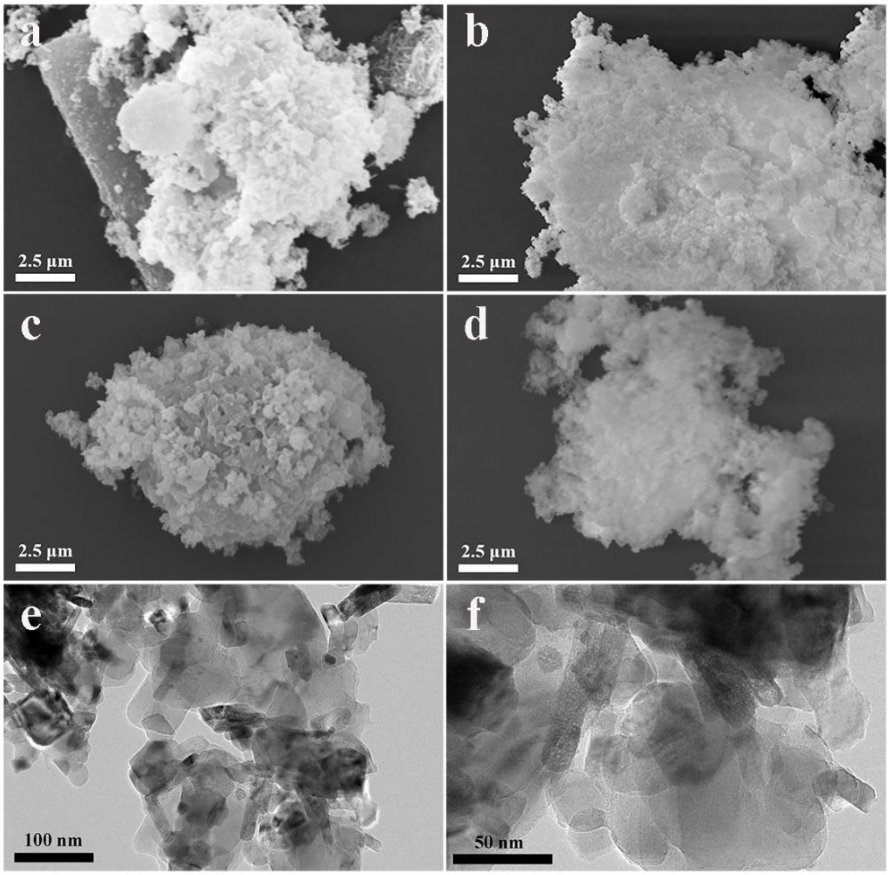

Fig. 14. SEM and TEM images of DFMs after 10 cycles of ICCU process: CeO_2-MgO (a), 2.5Ru/CeO_2-MgO (b), 5Ru/CeO_2-MgO (c, e, f) and 10Ru/CeO_2-MgO (d).

4. Conclusions

A novel ICCU process for carbon capture and methane production has been demonstrated using DFMs, which is a physical mixture of an inexpensive high-capacity MgO sorbent and CO_2 methanation catalyst (Ru supported on the CeO_2 nanorods) by the mass ratio of 2:1. In this ICCU

process, the regeneration of the sorbent and the conversion of cpatured CO_2 are carried out in a single reactor at the same intermediate temperature (300 ˚C) simultaneously, reducing the energy requirement for the sorbent regeneration. The produced CH_4 can be used based on existing infrastructure while the reduction of CO_2 emission is fulfilled. It is found that 10Ru/CeO_2-MgO exhibits highest CH_4 yield (7.07 mmol g^{-1}) and CO_2 conversion (89%) in the 1st cycle of ICCU process due to more oxygen vacanies are generated. However, 5Ru/CeO_2-MgO remains most oxygen vacanies caused by the metal-spport interaction compared to other DFMs and demonstrates the highset CH_4 yeild (3.36 mmol g^{-1}) and CO_2 conversion (79%) after 10 cycles of ICCU process.

Acknowledgements

The authors thank the financial support from National Natural Science Foundation of China (No. 21706050) and the China Scholarship Council (No. 201606450016). The authors also thank the funding from the European Union's Horizon 2020 research and innovation programme under the Marie Skłodowska-Curie Grant Agreement (No. 823745).

References

[1] M.A. Arellano-Treviño, Z. He, M.C. Libby, R.J. Farrauto, Catalysts and adsorbents for CO_2 capture and conversion with dual function materials: Limitations of Ni-containing DFMs for flue gas applications, J. CO2 Util. 31 (2019) 143-151.

[2] H. Guo, X. Kou, Y. Zhao, S. Wang, X. Ma, Role of microstructure, electron transfer, and coordination state in the CO_2 capture of calcium-based sorbent by doping (Zr-Mn), Chem. Eng. J. 336 (2018) 376-385.

[3] H. Sun, C.M. Parlett, M.A. Isaacs, X. Liu, G. Adwek, J. Wang, B. Shen, J. Huang, C. Wu, Development of Ca/KIT-6 adsorbents for high temperature CO_2 capture, Fuel 235 (2019) 1070-1076.

[4] N. Gao, K. Chen, C. Quan, Development of CaO-based adsorbents loaded on charcoal for CO_2 capture at high temperature, Fuel 260 (2020) 116411.

[5] M.S. Duyar, S. Wang, M.A. Arellano Trevino, R.J. Farrauto, CO_2 utilization with a novel dual function material (DFM) for capture and catalytic conversion to synthetic natural gas: An update, J. CO2 Util. 15 (2016) 65-71.

[6] L. Proaño, E. Tello, M.A. Arellano-Trevino, S. Wang, R.J. Farrauto, M. Cobo, In-situ DRIFTS study of two-step CO_2 capture and catalytic methanation over Ru,"Na_2O"/Al_2O_3 Dual Functional Material, Appl. Surf. Sci. 479 (2019) 25-30.

[7] F.N. Ridha, D.Y. Lu, R.T. Symonds, S. Champagne, Attrition of CaO-based pellets in a 0.1 MWth dual fluidized bed pilot plant for post-combustion CO_2 capture, Powder Technol. 291 (2016) 60-65.

[8] H. Sun, J. Wang, J. Zhao, B. Shen, J. Shi, J. Huang, C. Wu, Dual functional catalytic materials of Ni over Ce-modified CaO sorbents for integrated CO_2 capture and conversion, Appl. Catal. B: Environ. 244 (2019) 63-75.

[9] M.S. Duyar, M.A.A. Trevino, R.J. Farrauto, Dual function materials for CO_2 capture and conversion using renewable H_2, Appl. Catal. B: Environ. 168 (2015) 370-376.

[10] M.A. Arellano-Treviño, N. Kanani, C.W. Jeong-Potter, R.J. Farrauto, Bimetallic catalysts for CO_2 capture and hydrogenation at simulated flue gas conditions, Chem. Eng. J. (2019) 121953.

[11] G. Melaet, W.T. Ralston, C.S. Li, S. Alayoglu, K. An, N. Musselwhite, B. Kalkan, G.A. Somorjai, Evidence of highly active cobalt oxide catalyst for the Fischer-Tropsch synthesis and CO_2 hydrogenation, J. Am. Chem. Soc. 136(6) (2014) 2260-2263.

[12] L. Pastor-Pérez, F. Baibars, E. Le Sache, H. Arellano-Garcia, S. Gu, T. Ramirez Reina, CO_2 valorisation via reverse water-gas shift reaction using advanced Cs doped Fe-Cu/Al_2O_3 catalysts, J. CO2 Util. 21 (2017) 423-428.

[13] S.M. Kim, P.M. Abdala, M. Broda, D. Hosseini, C. Copéret, C. Müller, Integrated CO_2 Capture and Conversion as an Efficient Process for Fuels from Greenhouse Gases, ACS Catal. 8(4) (2018) 2815-2823.

[14] A. Al-Mamoori, A.A. Rownaghi, F. Rezaei, Combined Capture and Utilization of CO_2 for Syngas Production over Dual-Function Materials, ACS Sustain. Chem. Eng. 6(10) (2018) 13551-13561.

[15] N.M. Martin, P. Velin, M. Skoglundh, M. Bauer, P. Carlsson, Catalytic hydrogenation of CO_2 to methane over supported Pd, Rh and Ni catalysts, Catal. Sci. Technol. 7(5) (2017) 1086-1094.

[16] M. Tahir, B. Tahir, N.A.S. Amin, A. Muhammad, Photocatalytic CO_2 methanation over NiO/In_2O_3 promoted TiO_2 nanocatalysts using H_2O and/or H_2 reductants, Energ. Convers. Manage. 119 (2016) 368-378.

[17] X. Guo, Z. Peng, A. Traitangwong, G. Wang, H. Xu, V. Meeyoo, C. Li, S. Zhang, Ru nanoparticles stabilized by ionic liquids supported onto silica: highly active catalysts for low-temperature CO_2 methanation, Green Chem. 20(21) (2018) 4932-4945.

[18] M.S. Duyar, A. Ramachandran, C. Wang, R.J. Farrauto, Kinetics of CO_2 methanation over Ru/γ-Al_2O_3 and implications for renewable energy storage applications, J. CO2 Util. 12 (2015) 27-33.

[19] T. Sakpal, L. Lefferts, Structure-dependent activity of CeO_2 supported Ru catalysts for CO_2 methanation, J. Catal. 367 (2018) 171-180.
[20] F. Wang, S. He, H. Chen, B. Wang, L. Zheng, M. Wei, D.G. Evans, X. Duan, Active site dependent reaction mechanism over Ru/CeO_2 catalyst toward CO_2 methanation, J. Am. Chem. Soc. 138(19) (2016) 6298-6305.
[21] A. Bermejo-López, B. Pereda-Ayo, J.A. González-Marcos, J.R. González-Velasco, Mechanism of the CO_2 storage and in situ hydrogenation to CH_4. Temperature and adsorbent loading effects over Ru-CaO/Al_2O_3 and Ru-Na_2CO_3/Al_2O_3 catalysts, Appl. Catal. B: Environ. 256 (2019) 117845.
[22] H. Sun, C. Wu, B. Shen, X. Zhang, Y. Zhang, J. Huang, Progress in the development and application of CaO-based adsorbents for CO_2 capture-a review, Mater. Today Sustain. 1 (2018) 1-27.
[23] T. Harada, T.A. Hatton, Colloidal nanoclusters of MgO coated with alkali metal nitrates/nitrites for rapid, high capacity CO_2 capture at moderate temperature, Chem. Mater. 27(23) (2015) 8153-8161.
[24] T. Harada, F. Simeon, E.Z. Hamad, T.A. Hatton, Alkali metal nitrate-promoted high-capacity MgO adsorbents for regenerable CO_2 capture at moderate temperatures, Chem. Mater. 27(6) (2015) 1943-1949.
[25] Y. Qiao, J. Wang, Y. Zhang, W. Gao, T. Harada, L. Huang, T.A. Hatton, Q. Wang, Alkali nitrates molten salt modified commercial MgO for intermediate-temperature CO_2 capture: Optimization of the Li/Na/K ratio, Ind. Eng. Chem. Res. 56(6) (2017) 1509-1517.
[26] Y. Guo, S. Mei, K. Yuan, D. Wang, H. Liu, C. Yan, Y. Zhang, Low-Temperature CO_2 Methanation over CeO_2-Supported Ru Single Atoms, Nanoclusters, and Nanoparticles Competitively Tuned by Strong Metal-Support Interactions and H-Spillover Effect, ACS Catal. 8(7) (2018) 6203-6215.
[27] F. Wang, C. Li, X. Zhang, M. Wei, D.G. Evans, X. Duan, Catalytic behavior of supported Ru nanoparticles on the {1 0 0},{1 1 0}, and {1 1 1} facet of CeO_2, J. Catal. 329 (2015) 177-186.
[28] S. Wang, L. Zhao, W. Wang, Y. Zhao, G. Zhang, X. Ma, J. Gong, Morphology control of ceria nanocrystals for catalytic conversion of CO_2 with methanol, Nanoscale 5(12) (2013) 5582-5588.
[29] N. Wang, W. Qian, W. Chu, F. Wei, Crystal-plane effect of nanoscale CeO_2 on the catalytic performance of Ni/CeO_2 catalysts for methane dry reforming, Catal. Sci. Technol. 6(10) (2016) 3594-3605.
[30] A. Ciftci, D.M. Ligthart, P. Pastorino, E.J. Hensen, Nanostructured ceria supported Pt and Au catalysts for the reactions of ethanol and formic acid, Appl. Catal. B: Environ. 130 (2013) 325-335.

[31] X. Liu, B. Zhang, L. Xu, Noble metal catalyzed preparation of Ni_2P/α-Al_2O_3, Phys. Chem. Chem. Phys. 15(25) (2013) 10510-10514.

[32] K.A. Pokrovski, A.T. Bell, Effect of dopants on the activity of $Cu/M_{0.3}Zr_{0.7}O_2$ (M= Ce, Mn, and Pr) for CO hydrogenation to methanol, J. Catal. 244(1) (2006) 43-51.

[33] J. An, Y. Wang, J. Lu, J. Zhang, Z. Zhang, S. Xu, X. Liu, T. Zhang, M. Gocyla, M. Heggen, Acid-promoter-free ethylene methoxycarbonylation over Ru-clusters/ceria: the catalysis of interfacial Lewis acid–base pair, J. Am. Chem. Soc. 140(11) (2018) 4172-4181.

[34] X. Du, D. Zhang, L. Shi, R. Gao, J. Zhang, Morphology dependence of catalytic properties of Ni/CeO_2 nanostructures for carbon dioxide reforming of methane, J. Phys. Chem. C 116(18) (2012) 10009-10016.

[35] Z. Li, M. Li, J. Ashok, S. Kawi, NiCo@NiCo phyllosilicate@CeO_2 hollow core shell catalysts for steam reforming of toluene as biomass tar model compound, Energ. Convers. Manage. 180 (2019) 822-830.

[36] H. Huang, Q. Dai, X. Wang, Morphology effect of Ru/CeO_2 catalysts for the catalytic combustion of chlorobenzene, Appl. Catal. B: Environ. 158 (2014) 96-105.

[37] Z. Hu, X. Liu, D. Meng, Y. Guo, Y. Guo, G. Lu, Effect of ceria crystal plane on the physicochemical and catalytic properties of Pd/ceria for CO and propane oxidation, ACS Catal. 6(4) (2016) 2265-2279.

[38] S. Rönsch, J. Schneider, S. Matthischke, M. Schlüter, M. Götz, J. Lefebvre, P. Prabhakaran, S. Bajohr, Review on methanation-from fundamentals to current projects, Fuel 166 (2016) 276-296.

[39] J.A.H. Dreyer, P. Li, L. Zhang, G.K. Beh, R. Zhang, P.H.L. Sit, W.Y. Teoh, Influence of the oxide support reducibility on the CO_2 methanation over Ru-based catalysts, Appl. Catal. B: Environ. 219 (2017) 715-726.

[40] S. Tada, T. Shimizu, H. Kameyama, T. Haneda, R. Kikuchi, Ni/CeO_2 catalysts with high CO_2 methanation activity and high CH_4 selectivity at low temperatures, Int. J. Hydrogen Energy 37(7) (2012) 5527-5531.

[41] M. He, J. Ji, B. Liu, H. Huang, Reduced TiO_2 with tunable oxygen vacancies for catalytic oxidation of formaldehyde at room temperature, Appl. Surf. Sci. 473 (2019) 934-942.

[42] X. Wang, Y. Hong, H. Shi, J. Szanyi, Kinetic modeling and transient DRIFTS-MS studies of CO_2 methanation over Ru/Al_2O_3 catalysts, J. Catal. 343 (2016) 185-195.

[43] X. Du, D. Zhang, L. Shi, R. Gao, J. Zhang, Coke-and sintering-resistant monolithic catalysts derived from in situ supported hydrotalcite-like films on Al wires for dry reforming of methane, Nanoscale 5(7) (2013) 2659-2663.